Evolution of modes in a metal-coated nano-fiber

Junfeng Song,[1,2,*] Remo Proietti Zaccaria,[2,3] Guancai Dong,[2] Enzo Di Fabrizio,[3] M. B. Yu,[1] and G. Q. Lo[1]

[1]*Institute of Microelectronics, A*STAR (Agency for Science, Technology and Research), 11 Science Park Road, Singapore Science Park II, 117685 Singapore*
[2]*State Key Laboratory on Integrated opto-electronics, College of Electronic Science and Engineering, Jilin University, Changchun, 130023, China*
[3]*Italian Institute of Technology (IIT), NanoBioScience Laboratory, Genova, Italy*
**songjf@ime.a-star.edu.sg*

Abstract: We report on the evolution of modes in cylindrical metal/dielectric systems. The transition between surface plasmon polaritons and localized modes is documented in terms of the real and imaginary parts of the effective refractive index as a function of geometric and optical parameters. We show the evolution process of SPP and localized modes. New phenomena of coupling between SPP and core-like modes, and of mode gap and super-long surface plasmon polaritons are found and discussed. We conclude that both superluminal light and slow light can be solutions of metallically coated dielectric fibers.

OCIS codes: (240.6680) Surface plasmons; (130.2790) Guided waves; (060.2400) Fiber properties.

References and links

1. Y. Peng, X. Wang, and K. Kempa, "TEM-like optical mode of a coaxial nanowaveguide," Opt. Express **16**(3), 1758–1763 (2008).
2. J. Takahara, S. Yamagishi, H. Taki, A. Morimoto, and T. Kobayashi, "Guiding of a one-dimensional optical beam with nanometer diameter," Opt. Lett. **22**(7), 475–477 (1997).
3. A. S. Lapchuk, D. Shin, H. S. Jeong, C. S. Kyong, and D. I. Shin, "Mode propagation in optical nanowaveguides with dielectric cores and surrounding metal layers," Appl. Opt. **44**(35), 7522–7531 (2005).
4. U. Schröter and A. Dereux, "Surface plasmon polaritons on metal cylinders with dielectric core," Phys. Rev. B **64**(12), 125420 (2001).
5. U. Langbein, U. Trutschel, A. Unger, and M. Duguay, "Rigorous mode solver for multilayer cylindrical waveguide structures using constraints optimization," Opt. Quantum Electron. **41**(4), 223–233 (2009).
6. Y. Saito and P. Verma, "Imaging and spectroscopy through plasmonic nano-probe," Eur. Phys. J. Appl. Phys. **46**(2), 20101 (2009).
7. F. De Angelis, M. Patrini, G. Das, I. Maksymov, M. Galli, L. Businaro, L. C. Andreani, and E. Di Fabrizio, "A hybrid plasmonic-photonic nanodevice for label-free detection of a few molecules," Nano Lett. **8**(8), 2321–2327 (2008).
8. A. K. Sharma and B. D. Gupta, "Comparison of performance parameters of conventional and nano-plasmonic fiber optic sensors," Plasmonics **2**(2), 51–54 (2007).
9. F. De Angelis, G. Das, P. Candeloro, M. Patrini, M. Galli, A. Bek, M. Lazzarino, I. Maksymov, C. Liberale, L. C. Andreani, and E. Di Fabrizio, "Nanoscale chemical mapping using three-dimensional adiabatic compression of surface plasmon polaritons," Nat. Nanotechnol. **5**(1), 67–72 (2010).
10. A. Shinya, S. Mitsugi, E. Kuramochi, and M. Notomi, "Ultrasmall multi-channel resonant-tunneling filter using mode gap of width-tuned photonic-crystal waveguide," Opt. Express **13**(11), 4202–4209 (2005).
11. H. Zhao, R. P. Zaccaria, P. Verma, J. F. Song, and H. B. Sun, "Validity of the V parameter for photonic quasi-crystal fibers," Opt. Lett. **35**(7), 1064–1066 (2010).
12. P. Yeh, A. Yariv, and E. Marom, "Theory of Bragg fiber," J. Opt. Soc. Am. **68**(9), 1196–1201 (1978).
13. G. Ouyang, Y. Xu, and A. Yariv, "Theoretical study on dispersion compensation in air-core Bragg fibers," Opt. Express **10**(17), 899–908 (2002).
14. T. Ito and K. Sakoda, "Photonic bands of metallic systems. II. Features of surface plasmon polaritons," Phys. Rev. B **64**(4), 045117 (2001).
15. I. El-Kady, M. M. Sigalas, R. Biswas, K. M. Ho, and C. M. Soukoulis, "Metallic photonic crystals at optical wavelengths," Phys. Rev. B **62**(23), 15299–15302 (2000).
16. L. Novotny and C. Hafner, "Light propagation in a cylindrical waveguide with a complex, metallic, dielectric function," Phys. Rev. E Stat. Phys. Plasmas Fluids Relat. Interdiscip. Topics **50**(5), 4094–4106 (1994).
17. J. A. Buck, *Fundamentals of Optical Fibers* (Wiley-Interscience, 2004).
18. I. H. Malitson, "Interspecimen comparison of the refractive index of fused silica," J. Opt. Soc. Am. **55**(10), 1205–1209 (1965).

#152808 - $15.00 USD Received 18 Aug 2011; revised 22 Oct 2011; accepted 25 Oct 2011; published 23 Nov 2011

19. R. Adato and J. Guo, "Characteristics of ultra-long range surface plasmon waves at optical frequencies," Opt. Express **15**(8), 5008–5017 (2007).
20. X. L. Zhang, J. F. Song, G. Q. Lo, and D. L. Kwong, "The observation of super-long range surface plasmon polaritons modes and its application as sensory devices," Opt. Express **18**(21), 22462–22470 (2010).

1. Introduction

Surface plasmon polaritons (SPPs) are quasiparticles associated with a propagating electromagnetic field localized at the interface between a metal and a dielectric. SPPs originate from the coupling between incident photons and plasmons (oscillating ensemble of electrons) at the surface of metals. Metallic cylindric-like structures [1–5] with submicron diameters may be useful for applications such as near field scanning optical microscopy [6], or for employment in chemical and biologic sensor technology [7–9]. Furthermore, structures showing periodic arrangement have also been analyzed both in dielectric [10–13] and metallic configuration [14,15] for fiber/waveguides applications.

In this paper we investigate the evolution of modes in multilayer metal/dielectric cylindric structures. We will show that two kinds of modes can exist, an external SPP and an internal SPP/core mode. Furthermore, under particular circumstances, a bridging between these modes has been demonstrated [16]. Most importantly, when the geometrical/optical parameters are properly tuned, the rising of *mode-gap* (interspace cut-off) is observed. In these regions the existence of any kind of mode is forbidden. The model we consider is an ideal infinitely long dielectric/metal/dielectric submicron-fiber. Both the metallic and the dielectric parts are treated with a dispersion approach. In particular, in section 2, we will introduce the numerical method utilized for the present analysis. In section 3 we will discuss the dependence of the eigenmodes on the wavelength, radius, metal thickness, and background refractive index. Furthermore, we will discuss the coupling mechanisms between SPP- and core-like modes. In section 4, we will analyze the existence of virtually loss-free eigenmodes, named super-long SPP (SLSPP). In section 5, we shall report on the group velocity of the modes, and we will show the conditions for sub-luminal and super-luminal light speed. Finally, in section 6, we will give our conclusions.

2. Localized modes in submicron-fibers: numerical method

2.1 Determination of fiber modes

The sketch of a radial stratified fiber is shown in Fig. 1. The core of the fiber is named 1st layer, whereas the last N^{th} layer corresponds to the background media. In this model, any layer may show absorption, such as metal or some active media. Cylindrical coordinates are chosen in order to study the structure.

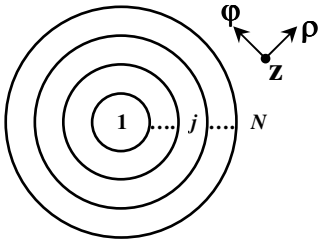

Fig. 1. Sketch of a multi-layer fiber. The cylindrical coordinates (ρ,φ,z) are shown.

The standard approach to solve this kind of structure starts by evaluating the components along the direction z of the electric- and magnetic- fields, e_z and h_z. They are expressed in Eq. (1) by means of the separation of variables method. In particular, the radial (ρ), azimuthal (φ) and axial (z) contribute are shown:

#152808 - $15.00 USD Received 18 Aug 2011; revised 22 Oct 2011; accepted 25 Oct 2011; published 23 Nov 2011

$$\begin{pmatrix} e_z^{(j)} \\ \overline{h}_z^{(j)} \end{pmatrix} = \sum_{m,l=-\infty}^{+\infty} \begin{pmatrix} e_{m,l,z}^{(j)}\left(\overline{\rho}\, n_{m,l,t}^{(j)}\right) \\ \overline{h}_{m,l,z}^{(j)}\left(\overline{\rho}\, n_{m,l,t}^{(j)}\right) \end{pmatrix} \exp\left(im\varphi\right)\exp\left(in_{m,l,z}\overline{z} - i\omega t\right) \tag{1}$$

with

$$\begin{pmatrix} e_{m,l,z}^{(j)}\left(\overline{\rho}\, n_{m,l,t}^{(j)}\right) \\ \overline{h}_{m,l,z}^{(j)}\left(\overline{\rho}\, n_{m,l,t}^{(j)}\right) \end{pmatrix} = H_m^{(1)}\left(\overline{\rho}\, n_{m,l,t}^{(j)}\right)\mathbf{A}_{m,l}^{(j)} + H_m^{(2)}\left(\overline{\rho}\, n_{m,l,t}^{(j)}\right)\mathbf{B}_{m,l}^{(j)} \tag{2}$$

where $\overline{\rho} = k_0\rho$, $\overline{z} = k_0 z$ and $\overline{h} = h\left(\omega\mu_0/k_0\right)$. The quantity ω is the angular frequency, k_0 is the wave number in vacuum and μ_0 is the permeability in free space. Furthermore, j denotes the j^{th} concentric layer and m is an integer which represents the order in the azimuthal coordinate (associated to the angle φ). Generally, the solutions include the guided (localized) modes and radiation modes. l is for extinguishing every solution. It depends on azimuthal order m. However, in this paper, we are focusing on the localized individual eigenmodes. For simplified expression, we ignore l in following discussion. The contribute $\exp\left(in_{m,z}\overline{z} - i\omega t\right)$ indicates light propagating along z direction with an effective refractive index given by $n_{m,z}$. Its value is complex if any of the layers possess absorptive characteristics. It is important to notice that $n_{m,z}$ is layer independent, namely it does not depend on the parameter j. The relation relating the transversal and axial (z-axis) effective index is shown in Eq. (3), where $\varepsilon^{(j)}$ and $\mu^{(j)}$ are the relative permittivity and permeability of the j^{th} layer, respectively . Because $n_{m,z}$ is a complex quantity, this relation implies $n_{m,t}$ to be complex, too:

$$\left(n_{m,t}^{(j)}\right)^2 + n_{m,z}^2 = \varepsilon^{(j)}\mu^{(j)} \tag{3}$$

Both the z-axis distribution functions $e_{m,z}$ and $\overline{h}_{m,z}$ satisfies the Helmholtz equation. They are described by a linear combination of m-order Bessel functions H_m (specifically Hankel functions, superscript (1) and (2) denote first and second kind of Hankel function.), as in Eq. (2). **A** and **B** are coefficients of the form $\mathbf{A} = (a_1, a_2)^T$, $\mathbf{B} = (b_1, b_2)^T$, respectively. From the components along z of the electric and magnetic field, we can calculate their radial and azimuthal components. The procedure is shown in Eqs. (4) and (5) [17]:

$$\begin{pmatrix} e_{m,\rho}^{(j)} \\ \overline{h}_{m,\rho}^{(j)} \end{pmatrix} = \frac{1}{\left(n_{m,t}^{(j)}\right)^2}\left[in_{m,z}\frac{\partial}{\partial\overline{\rho}} + \begin{pmatrix} 0 & -\mu^{(j)} \\ \varepsilon^{(j)} & 0 \end{pmatrix}\frac{m}{\overline{\rho}}\right]\begin{pmatrix} e_{m,z}^{(j)} \\ \overline{h}_{m,z}^{(j)} \end{pmatrix} \tag{4}$$

$$\begin{pmatrix} e_{m,\varphi}^{(j)} \\ \overline{h}_{m,\varphi}^{(j)} \end{pmatrix} = \frac{1}{\left(n_{m,t}^{(j)}\right)^2}\left[-m\frac{n_{m,z}}{\overline{\rho}} + i\begin{pmatrix} 0 & -\mu^{(j)} \\ \varepsilon^{(j)} & 0 \end{pmatrix}\frac{\partial}{\partial\overline{\rho}}\right]\begin{pmatrix} e_{m,z}^{(j)} \\ \overline{h}_{m,z}^{(j)} \end{pmatrix} \tag{5}$$

Necessary condition to obtain localized modes along the transversal direction states that all the elements of electro-magnetic field must decay in last layer. This is possible only under the assumption that the imaginary part of $n_{m,t}^{(j)}$ associated to the last layer is a positive quantity. In fact, under these conditions the solution of the Bessel equation for a cylindric system would be given only by the first term in Eq. (2) (the $H_m^{(1)}$ term) which decays by increasing $\overline{\rho}$. Substituting Eq. (2) into Eq. (4) and (5), from the continuity relations at the interface of the electro-magnetic field and by means of the transfer matrix method, we can obtain the relations between two adjacent layers:

$$\mathbf{M}(j, j)\begin{pmatrix} \mathbf{A}_m^{(j)} \\ \mathbf{B}_m^{(j)} \end{pmatrix} = \mathbf{M}(j+1, j)\begin{pmatrix} \mathbf{A}_m^{(j+1)} \\ \mathbf{B}_m^{(j+1)} \end{pmatrix}$$

#152808 - $15.00 USD Received 18 Aug 2011; revised 22 Oct 2011; accepted 25 Oct 2011; published 23 Nov 2011

where matrix **M** is a 4 by 4 matrix with 4 matrix components $\mathbf{M}_{\alpha,\beta}$. $\mathbf{M}_{\alpha,\beta}$ is a 2 by 2 matrix. α and β denote 1 or 2. j and $j + 1$ are variable parameters in matrix **M** denote j^{th} and $(j + 1)^{\text{th}}$ layers. Sub-elements matrix $\mathbf{M}_{\alpha,\beta}$ can be described as

$$\mathbf{M_{11}}\left(q,p\right)=H_m^{(1)}\left(n_{m,t}^{(q)}\overline{R}_p\right)\mathbf{I} \tag{6a}$$

$$\mathbf{M_{12}}\left(q,p\right)=H_m^{(2)}\left(n_{m,t}^{(q)}\overline{R}_p\right)\mathbf{I} \tag{6b}$$

$$\mathbf{M_{21}}\left(q,p\right)=\frac{1}{n_{m,t}^{(q)}\overline{R}_p}\left[-n_z H_m^{(1)(+)}\left(n_{m,t}^{(q)}\overline{R}_p\right)\mathbf{I}+H_m^{(1)(-)}\left(n_{m,t}^{(q)}\overline{R}_p\right)i\begin{pmatrix}0 & -\mu^{(q)}\\ \varepsilon^{(q)} & 0\end{pmatrix}\right] \tag{6c}$$

$$\mathbf{M_{22}}\left(q,p\right)=\frac{1}{n_{m,t}^{(q)}\overline{R}_p}\left[-n_z H_m^{(2)(+)}\left(n_{m,t}^{(q)}\overline{R}_p\right)\mathbf{I}+H_m^{(2)(-)}\left(n_{m,t}^{(q)}\overline{R}_p\right)i\begin{pmatrix}0 & -\mu^{(q)}\\ \varepsilon^{(q)} & 0\end{pmatrix}\right] \tag{6d}$$

where q and p replace j (or $j + 1$) as first and second variable parameters in matrix **M.**. The $H_m^{(1\,or\,2)(\pm)}\left(x\right)=\frac{1}{2}\left[H_{m-1}^{(1\,or\,2)}\left(x\right)\pm H_{m+1}^{(1\,or\,2)}\left(x\right)\right]$, $\overline{R}_p$ is the radius of the p-layer and **I** is 2 by 2 unit matrix.

The next step, given by Eq. (7), is the calculation of the transition matrix connecting the j^{th} and $(j + 1)^{\text{th}}$ layer. By applying this approach to all the layers, we can obtain the total transition matrix as in Eq. (8):

$$\mathbf{M}^{-1}\left(j+1,j\right)\mathbf{M}\left(j,j\right)\begin{pmatrix}\mathbf{A}_m^{(j)}\\ \mathbf{B}_m^{(j)}\end{pmatrix}=\mathbf{T}_j^{j+1}\begin{pmatrix}\mathbf{A}_m^{(j)}\\ \mathbf{B}_m^{(j)}\end{pmatrix}=\begin{pmatrix}\mathbf{A}_m^{(j+1)}\\ \mathbf{B}_m^{(j+1)}\end{pmatrix} \tag{7}$$

$$\mathbf{T}_{N-1}^{N}\cdots\mathbf{T}_{j-1}^{j}\cdots\mathbf{T}_1^2\begin{pmatrix}\mathbf{A}_m^{(1)}\\ \mathbf{B}_m^{(1)}\end{pmatrix}=\prod_{j=1}^{N-1}\mathbf{T}_j^{j+1}\begin{pmatrix}\mathbf{A}_m^{(1)}\\ \mathbf{B}_m^{(1)}\end{pmatrix}=\mathbf{T}\begin{pmatrix}\mathbf{A}_m^{(1)}\\ \mathbf{B}_m^{(1)}\end{pmatrix}=\begin{pmatrix}\mathbf{A}_m^{(N)}\\ \mathbf{B}_m^{(N)}\end{pmatrix} \tag{8}$$

In the first layer (the fiber core) the coefficients $\mathbf{A}_m^{(1)}$ and $\mathbf{B}_m^{(1)}$ must be equal to each other. The reason is easily explained by noticing the expression describing the field in the core region which is given by the first kind of Bessel function:

$$J_m\left(x\right)=\left[H_m^{(1)}\left(x\right)+H_m^{(2)}\left(x\right)\right]\Big/2. \tag{9a}$$

To realize a confined field a decay behavior must be satisfied in the most external layer which is obtained by

$$\mathbf{B}_m^{(N)}=0 \tag{9b}$$

Inserting Eqs. (9)a) and (9b) into Eq. (8), and noting that $\mathbf{A}_m^{(1)} = \mathbf{B}_m^{(1)}$, we obtain

$$\left(\mathbf{T}_{21}+\mathbf{T}_{22}\right)\mathbf{A}_m^{(1)}=0 \tag{10}$$

Non-trivial solution is possible if

$$\left\|\mathbf{T}_{21}+\mathbf{T}_{22}\right\|=0 \tag{11}$$

Equation (11) is the characteristic equation of the system. Solving it allows the determination of the complex effective index $n_{m,z}$. Finally, we can determine the spatial distributions of the electromagnetic field.

Regarding the numerical solving method of Eq. (11), a stepped reducing search-area method is adopted. We set an area of $n_{m,z}$ in a two dimensional complex plane, then solve Eq.

#152808 - $15.00 USD Received 18 Aug 2011; revised 22 Oct 2011; accepted 25 Oct 2011; published 23 Nov 2011

(11), and find $n_{m,z}$ to minimize the left side of Eq. (11) close to zero. Reduce search area around this value, and repeat searching until it meets the accuracy requirement.

For following discussion, we fix the m = 1 for example, and ignore the m in following discussion, unless otherwise specified.

2.2 Materials modeling

In the following analysis a combination of SiO_2, silver, and air is used to define a metallic fiber. We assume that both SiO_2 and Ag are dispersive media. We use the Sellmeier formulation to define the dielectric constant of SiO_2 [18]:

$$\varepsilon_{SiO_2} = 1 + \frac{A\lambda^2}{\lambda^2 - \lambda_1^2} + \frac{B\lambda^2}{\lambda^2 - \lambda_2^2} + \frac{C\lambda^2}{\lambda^2 - \lambda_3^2} \tag{12}$$

where

$$A = 0.6961663, \quad B = 0.4079426, \quad C = 0.8974794,$$

$$\lambda_1 = 0.0684043, \quad \lambda_2 = 0.1162414, \quad \lambda_3 = 9.896161.$$

Similarly, for silver,

$$\varepsilon_{Ag} = \left(n_{Ag} + i\kappa_{Ag}\right)^2 \tag{13}$$

where

$$n_{Ag} = 0.17861 + \lambda\left(0.0591 + 0.05859\lambda\right)$$
$$\kappa_{Ag} = 7.33428\lambda - 0.19444$$

The wavelength λ is taken in micrometers. Equations (12) and (13) require a wavelength larger than 0.4 μm and smaller than 4 μm.

3. Modes evolution

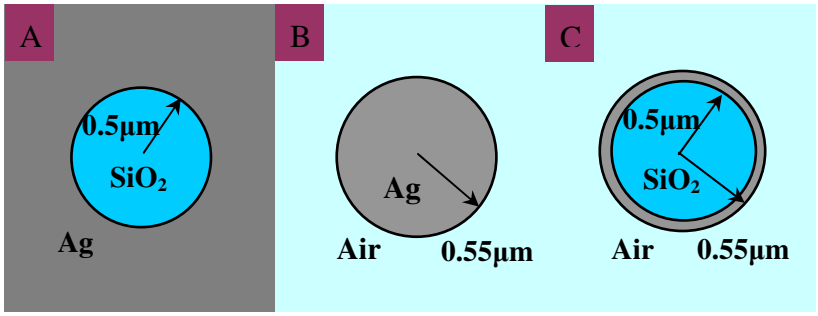

Fig. 2. Sketch of three kinds of metallic fibers: (A), dieletric core covered by an infinitely extended layer of metal; (B), metal covered by infinitely extended layer of dielectric; (C), thin metal film is located in between two dielectrics.

We will consider three different situations to model the behavior of both SPPs and localized modes on cylindric-like structures with infinite length. In Fig. 2 the three models are shown. Specifically, the type-A structure defines a cylinder made of silica (SiO2), with radius R = 0.50 μm surrounded by silver. Similarly, the case B shows a silver cylinder with radius R = 0.55 μm immerse in air background. Finally, the case C is a combination of the previous two: a cylinder with silica core of radius Rc = 0.50 μm is coated with 50 nm of silver. The system is surrounded by air. Throughout this paper, unless otherwise specified, we will consider the azimuthal number m = 1, since it represents the symmetry of single mode fibers.

#152808 - $15.00 USD Received 18 Aug 2011; revised 22 Oct 2011; accepted 25 Oct 2011; published 23 Nov 2011

3.1 Wavelength dependence

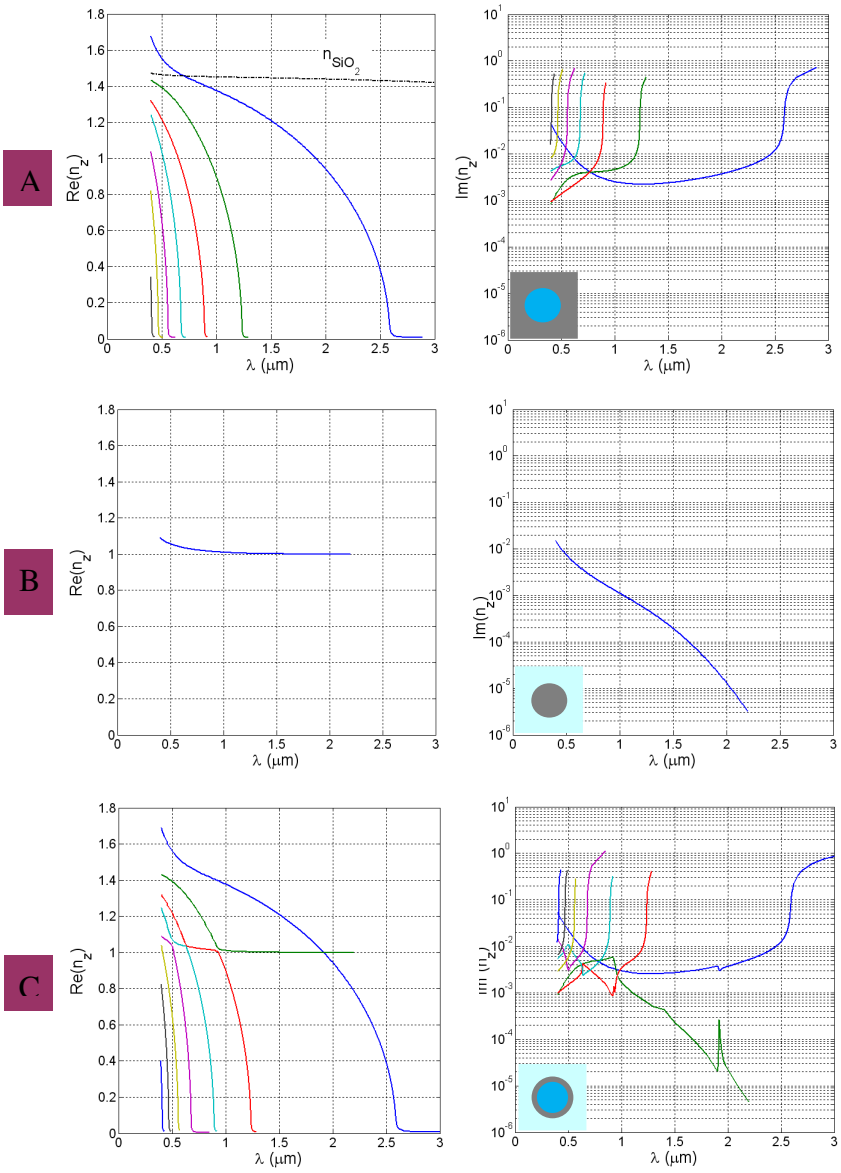

Fig. 3. The transmission constants for type-A, B and C structures. The real and imaginary parts of the refractive index are showed in the left and right columns, respectively. The azimuthal number m is equal to 1. The refractive index of silicon dioxide is shown in type-A figure (dashed line). Different colors are associated to different radial numbers, namely different modes. From right to left we move from the fundamental to higher order modes.

The real and imaginary parts of the effective refractive index n_z associated to different modes are shown in Figs. 3A, 3B and 3C. In all cases the real part decreases by increasing the wavelength. The refractive index of core SiO_2 is drawn in Fig. 3A (dashed line). The colors denote different modes, each associated to a different radial number. The order mode increases scrolling the figures from right to left. For the type-A structure, when the wavelength is shorter than 0.693μm, the real part of n_z associated to the fundamental mode

#152808 - $15.00 USD Received 18 Aug 2011; revised 22 Oct 2011; accepted 25 Oct 2011; published 23 Nov 2011

(blue line) is bigger than the refractive index of silica. The mode is then an internal surface plasmon mode. The maximum light field is located at the interface between metal and SiO_2. On the other hand, the minimum in intensity is at the center of the dielectric core. z direction Poynting vector is chosen for showing intensity distributions. Poynting vector is defined as $\mathbf{S} = 0.5\mathrm{Re}(\mathbf{E} \times \mathbf{H}^*)$. This is clearly shown in Fig. 4(a) where $\lambda = 0.5$ μm has been chosen. A phenomenological explanation rises from considering that the effective refractive index of the fundamental mode is higher than SiO_2. The field is then pushed out from the dielectric core towards its own edges, resulting in an internal-like SPP mode. Figure 3A also shows no intersections among the modes in the graph associated to the real part of the refractive index, intersections otherwise present in the imaginary part index. With wavelength increasing, the inner SPP mode, two segments will extend to center. Finally, fundamental mode becomes a localized mode, with maximum intensity of the field at the center of the dielectric core. No SPP features are present any longer, as is shown in Fig. 4(b). Similarly, the higher order modes have an effective refractive index always below SiO_2, which localizes them mainly in the core for any considered wavelength.

For the type-B structure, Fig. 3B shows the existence of only one single surface plasmon polariton mode. This is motivate by having an open structure, namely no spatially confined regions supporting modes exist in it (similarly to a flat metal/dielectric interface). By increasing the wavelength, the value of $\mathrm{Im}(n_z)$ decreases, which is opposite to the behavior showed by the imaginary part of the refractive index of Silver bulk, as shown in Eq. (13). It implies that this kind of mode tends to propagate along the cylinder for longer distances by increasing the wavelength (the same happens for flat metal/dielectric interfaces). This is physically supported by the fact that the refractive index of the mode tends to the unity (the refractive index of the surrounding medium), as graphically shown in Fig. 4(c). This mode, being then SPP-like, travels mostly in the dielectric which dramatically reduces its absorption.

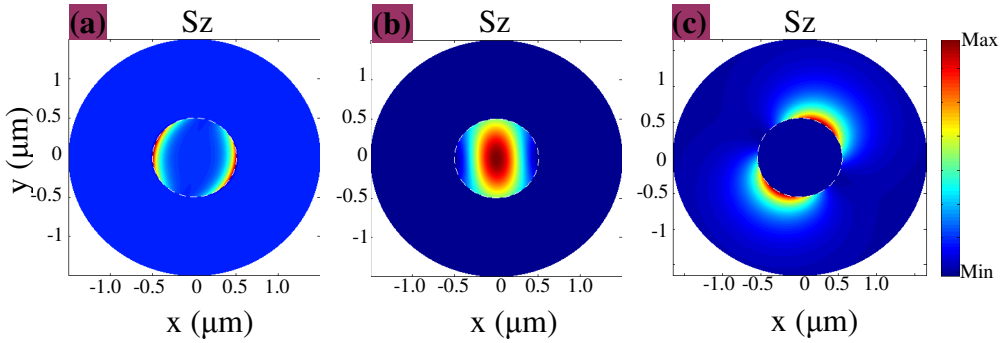

Fig. 4. z-component of the Poynting vector associated to the fundamental mode for the type-A structure at (a) $\lambda = 0.5$ μm. It is an internal SPP-like mode; (b) $\lambda = 2.0$ μm. It is a core mode. (c): type-B structure at $\lambda = 1.0$ μm. The SPP mode is mostly localized in the dielectric (external SPP mode).

Moving on to the type-C structure, we can notice that the graphs in Fig. 3C combine the dispersion relations from type-A and type-B structures. External surface plasmon modes (Fig. 3B) transversally *cut* the dispersion relation of the type-A structure. The intersection points correspond to two-modes overlapping spots. In the wavelength region close to 1.917 μm, the external SPP mode (green line) crosses the fundamental internally localized mode (blue line). However, the two modes are not degenerative because of the strong difference in the imaginary parts of the refractive indexes. This determines almost no change in the behavior of the fundamental mode when compared to the type-A structure, namely the mode maintains a core localized distribution. On the other hand, if we look at the first excited mode (green line) around $\lambda = 1.917$ μm, the mode evolves quickly from an external SPP-like shape to internal-core like to retake, for λ bigger than 1.917 μm, the external SPP-like form. The different behavior between the fundamental (blue line) and first excited mode (green line) can be well

#152808 - $15.00 USD Received 18 Aug 2011; revised 22 Oct 2011; accepted 25 Oct 2011; published 23 Nov 2011

explained looking at the imaginary part of the effective refractive index as in Fig. 3C. In fact, around the critical value of λ = 1.917 μm, the fundamental mode does not show almost any change while the first excited mode presents a strong Fano oscillation which is associated to an increase of loss. Physically this corresponds to the shift of the field distribution from the external dielectric region (air) to the internal one (SiO_2), that is the mode is no longer a SPP-like but core-like. Finally we notice that by increasing the wavelengths the loss tends to increase for the core modes. On the other hand, both the internal (type-A) and external (type-B) SPP modes show a strong decrease of the loss by increasing the wavelength. This will play an important role when later on we will discuss the super-long range SPP.

Figure 5 shows three snapshots at 400 nm, 640 nm and 930 nm. They are Poynting vector z component for the third dispersion line (red line) of the type-C structure as in Fig. 3C. Clearly the mode starts with a core-like distribution, to evolve into an external SPP-like shape at around 640 nm, to retake a core-like form around 930 nm. This swinging between SPP and core modes is due to external SPP mode and core-like mode coupled together. Original crossing dispersion relation curve, crossing point be split as two. Media 1 display the modes evolution process from core-like shape to external SPP-like shape, and tune back core-like shape again, with increasing wavelength.

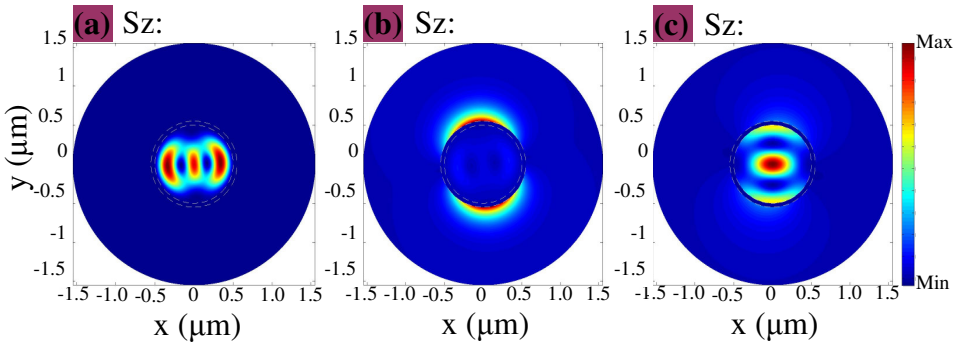

Fig. 5. Poynting vector along z direction (S_z) of the mode is denoted by red line in Fig. 3C (Media 1). Shown is the evolution of the mode distribution by changing the wavelength from 400 nm to 930 nm. Both core-like and SPP-like shapes are taken by the mode.

In fact, one of the most important differences among fibers with real and complex (leaky) effective refractive index is the mode cut-off. The former have modes each characterized by a particular value of the wavelength at n_z = 0, whereas the latter show no similar cut-off. Indeed, as shown in Figs. 3A and 3C, when the real part of n_z is close to 0, the dispersion curves suddenly tend to longer wavelengths and the associated modes show a core-like shape. When this happens, we observe a marked increase of the mode attenuation, associated to a sudden increase of the imaginary part of the refractive index.

3.2 Core radius dependence

Similarly to conventional step-index fibers, also for the type-C structure the number of supported eigenmodes increases with the radius of the core. For example, at the wavelength of 1.55 μm and thickness of silver equal to 50 nm, Figs. 6(a) and 6(b) show the real and imaginary parts of the axial effective refractive index vs. the radius of the core R_c, respectively. Once again, an external SPP curve *cuts* the internal modes. External SPP can then be seen as bridges connecting two different internal modes. When R_c reaches zero, which means to fall in the type-B structure, only one mode survives (green line) similarly to Fig. 3B. As general behavior, the loss decreases with increasing the radius of core. However, for SPP the loss is small even at small radius. Let us focus on the red line. Figures 6(c) and 6(d) show a gap-mode for R_c just above 0.86 μm. In fact, for these values of the core radius, the imaginary part of n_z is not defined. This phenomenon was recently reported for planar structures [19,20], and was referred as interspaces cut-off region. We can see how, at the

#152808 - $15.00 USD Received 18 Aug 2011; revised 22 Oct 2011; accepted 25 Oct 2011; published 23 Nov 2011

edges of this interspaced region, the imaginary part of n_z tends to values very close to 0. This result, which physically means no-loss eigenmodes, might sounds quite interesting considering that we are dealing with absorptive materials such as metals. From a mathematical point view it corresponds to a real solution of a more general complex matrix. In section 4 we shall refer to these kinds of modes as super-long SPP.

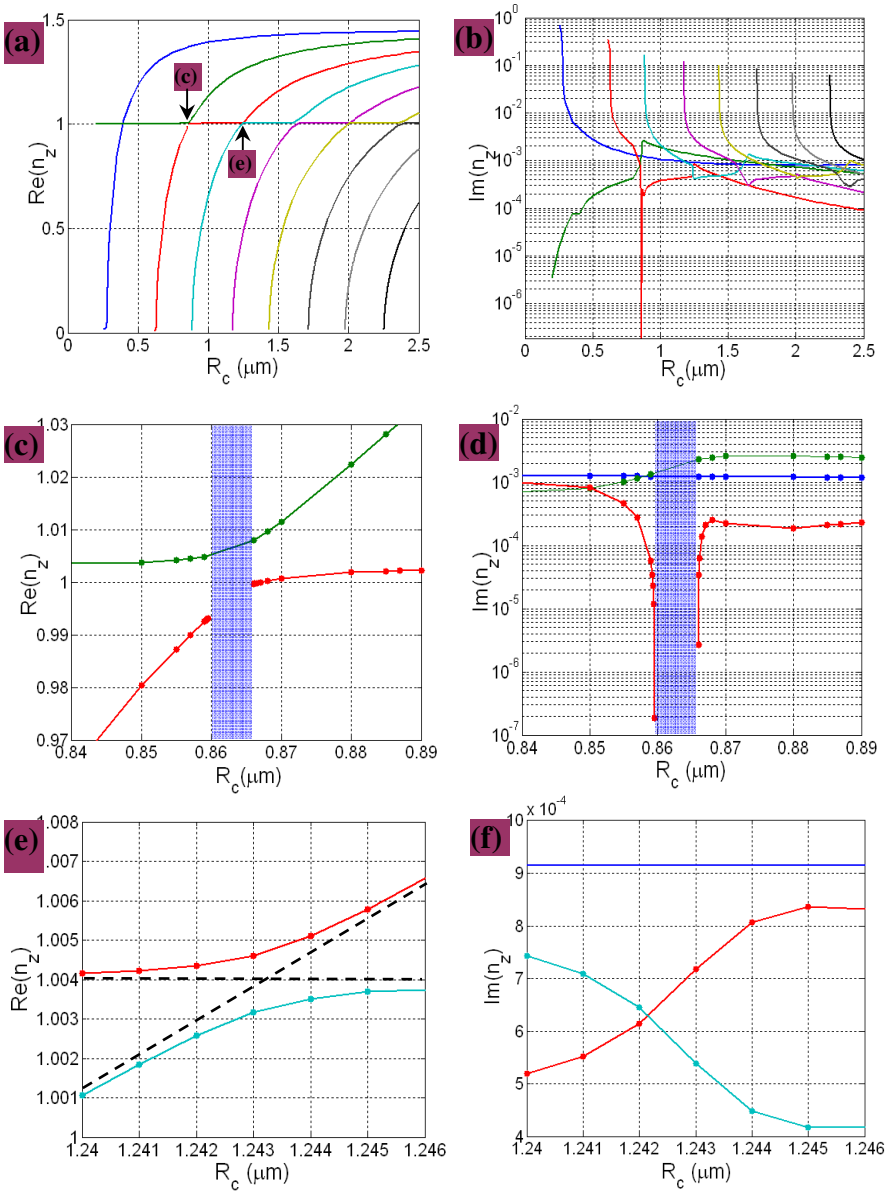

Fig. 6. The model was the type-C structure with thickness of the silver ring equal to 0.5 μm and wavelength fixed at 1.55 μm. (a) and (b) show the real- and imaginary- part of the axial effective refractive index vs. core radius, respectively. (c) and (d) are the close-up graphs of (a) and (b) in the range from 0.84 μm to 0.89 μm. (e) and (f) show the relation between 1.24 μm to 1.246 μm. See Media 2.

Similar to Fig. 3C, the external SPP and internal core-like modes couple one another. This is clearly shown in Figs. 6(e) and (f) by red and light blue lines, where the mode evolution is

#152808 - $15.00 USD Received 18 Aug 2011; revised 22 Oct 2011; accepted 25 Oct 2011; published 23 Nov 2011

from core-like mode to SPP, shown by light-blue line, and the opposite behavior is shown by the red line. Other words, the modes coupling effect change trace of dispersion relationship. The dished line in Fig. 6(e) illustrates show the original traces. And this means that, for this kind of fiber, if core side increases very slowly, the light can tunnel the thin metal cladding layer from inside to outside, or conversely. Media 2 displays this evolutionary process.

3.3 Dependence on thickness of the metal cladding layer

In this section we investigate the effect of the metal layer thickness on the modes for the type C structure. The radius of the dielectric core is fixed at the values both 0.3 μm and 0.5 μm. The wavelength is chosen equal to 1.55 μm. When the thickness h of the silver cladding layer reaches zero, the structure becomes a conventional dielectric nano-fiber. Here we introduce the propagation length $L_\tau = 1/2k_0\mathrm{Im}(n_z)$, as shown in Fig. 7(b). It represents the distance covered by the light before decaying to $1/e$ (~4.34 dB) of its initial value.

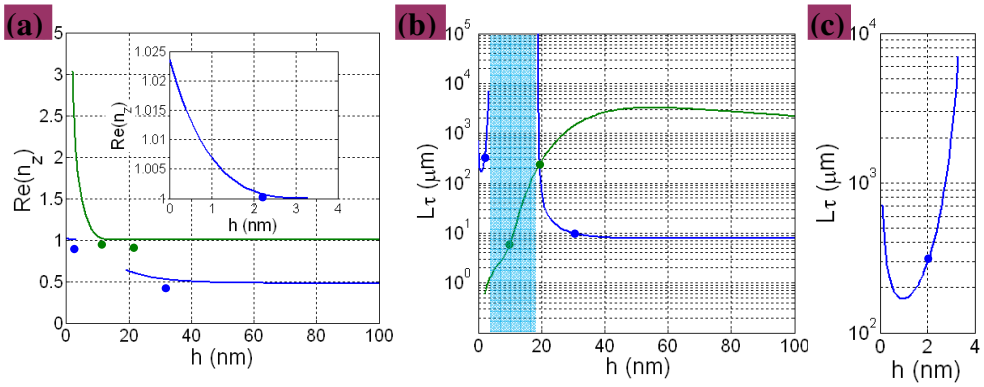

Fig. 7. (a) and (b) are the dispersion relation and the propagation length versus the thickness of the silver ring, respectively (the type-C structure is considered). Same color in the figures means same mode. (c) a particular of the blue line in (b). The radius of the SiO_2 core was taken equal to 0.30 μm and λ = 1.55 μm. The dots indicate the calculated mode profiles as in Fig. 8. See Media 3.

The green line in Fig. 7 is associated with a mode which, for small h, shows an effective refractive index even higher than core SiO_2. This implies that the mode is formed by a combination of intra- and extra-SPP contributes. In particular, these terms will exist mainly close to the metal interfaces due to the high effective refractive index induced optical filed fast decay from interface, in both side of core- and cladding- layers. By increasing the thickness h, we observe a reduction of the mode index, which reaches the constant value of 1 (the refractive index of the background) at around 10 nm. Of the two initial internal and external contributes to the field, only the external SPP is left, as shown in Figs. 8(a) and (b). Media 3 displays the modes evolution process.

The blue lines in Figs. 7(a) and (b) show a gap-mode between h = 3.5 nm and h = 19.1 nm, when the SiO_2 core is equal to 0.30 μm. The effective index is from 1.0236 (h = 0 nm) to the background index (h = 3.5 nm; see the inset in Fig. 7(a)). Figures 8(c) and 8(d) show the field profile at the edges of the gap-mode. For h = 2 nm, the mode is a combination of external SPP and core contributes. For h = 30 nm, the SPP part disappears and the mode covers the core area, which is consistent with the reduction of the effective refractive index n_z.

In terms of propagation length the two modes behave in a quite different way. In fact, the green line increases up to about h = 50 nm at which point it starts decreasing, whereas the blue line shows three steps: a U-like shape as in Fig. 7(c) for the first few nanometers, then a fast decrease and finally a constant value is reached. The most important information raising from L_τ are its high values at the edges of the gap. This, once again, seems to lead to the possibility of having modes which can virtually travel indefinitely in space.

#152808 - $15.00 USD Received 18 Aug 2011; revised 22 Oct 2011; accepted 25 Oct 2011; published 23 Nov 2011

When the radius of the SiO_2 core is changed to R_c = 0.5 μm, the situation is described by Fig. 9. In this case no gap-mode is found. SPP and core-like modes are shown in green and blue, respectively. The SPP mode tends to Re(n_z) = 1, namely the field is found on the background material. This is demonstrated in Fig. 10(a). The real part of n_z for the core-like mode is higher than the SPP mode, which is the opposite of the situation described in Fig. 7. This general behavior is well consistent with Fig. 6(a). From Figs. 7(b) and 9(b) we can see that the external SPP show lower transmission loss in submicron structures than the core-like modes.

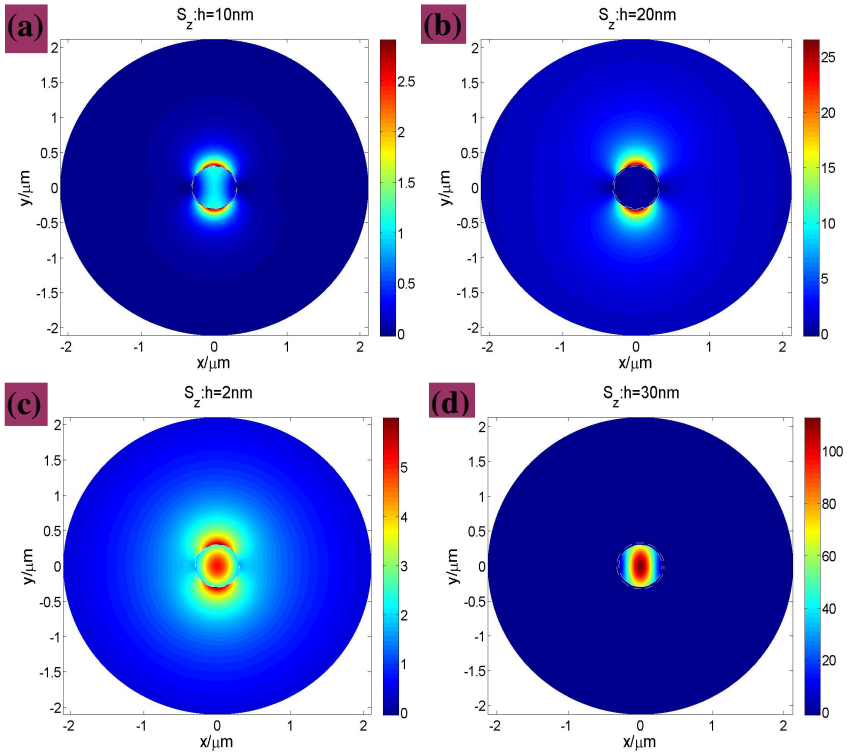

Fig. 8. Distribution of the Poynting vector S_z associated with the modes in Fig. 7: (a) h = 10 nm, green line; (b) h = 20 nm, green line; (c) h = 2 nm, blue line; (d) h = 30 nm, blue line. These fields were calculated by considering the terms with azimuthal number m = + 1 and m = –1.

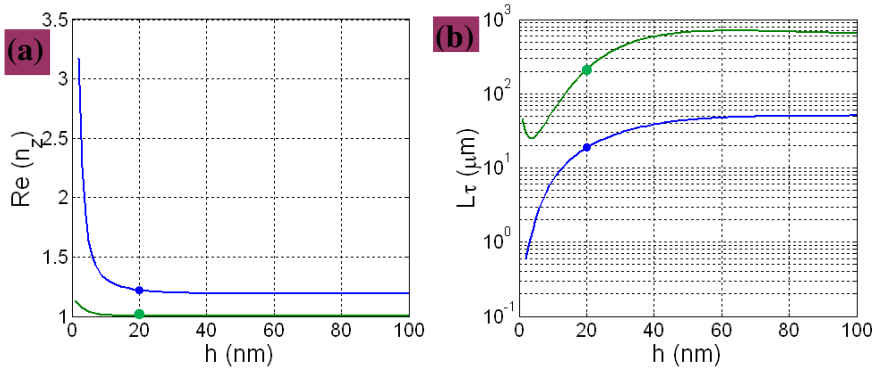

Fig. 9. (a) and (b) are the dispersion relation and the propagation length versus the thickness of the silver ring, respectively (the type-C structure is considered). Same color in the figures means same mode. The radius of the SiO_2 core was taken equal to 0.5μm and λ = 1.55 μm. The dots indicate the calculated mode profiles as in Fig. 10.

#152808 - $15.00 USD Received 18 Aug 2011; revised 22 Oct 2011; accepted 25 Oct 2011; published 23 Nov 2011

3.4 Dependence on the background index

Until now no considerations have been made on the role played by the refractive index of the background. In all our calculations (for the type-C structure) its value was always assumed equal to 1. However, in view of some applications such as gas and liquid sensor, we need to proceed evaluating the influence that the background might have on the overall behavior of the cylindric modes. Similarly to the previous section, we will employ R_c = 0.30 and 0.50 μm. Furthermore, we have chosen the wavelength λ = 1.55 μm and the metal ring thickness h = 50 nm. In Fig. 11 the radius R_c = 0.30 μm is considered. We see that both Re(n_z) and Im(n_z) for

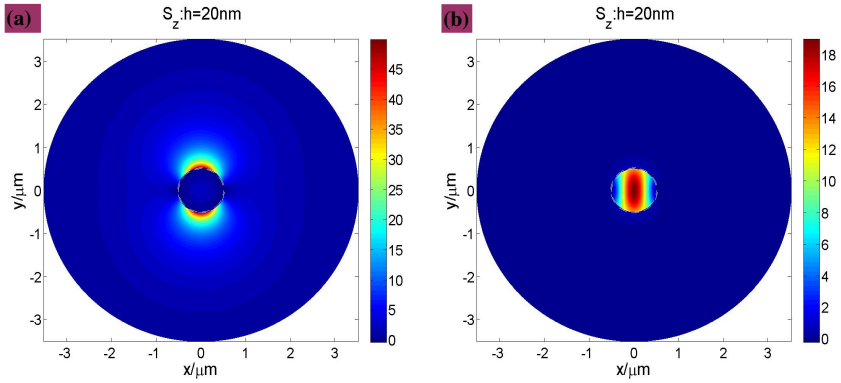

Fig. 10. (a) and (b) correspond to the S_z distribution for the green and blue line in Fig. 9, respectively. Silver thickness h = 20 nm is taken.

external SPP (green line) increase with the refractive index of the background (n_b). This phenomenon can be explained by considering the model of a simple planar surface plasmonic mode. In fact, for planar metal/dielectric SPP, the propagation index is described in Eq. (14). For the specific case of silver at wavelength λ = 1.55 μm, Eq. (14) is reduced to the expression described in Eq. (15). The real part of n_z approaches a linear function of n_b, whereas the imaginary part of n_z shows a cubic dependence on n_b:

$$n_{pls} = \sqrt{\frac{\varepsilon_b \varepsilon_m}{\varepsilon_b + \varepsilon_m}} \cong n_b - \frac{n_b^3}{2\,\mathrm{Re}(\varepsilon_m)} + \frac{i}{2}\frac{n_b^3}{\mathrm{Re}(\varepsilon_m)}\frac{\mathrm{Im}(\varepsilon_m)}{\mathrm{Re}(\varepsilon_m)} \tag{14}$$

$$n_{pls} = n_b + 0.004 n_b^3 + 2.954\times 10^{-4} i n_b^3 \tag{15}$$

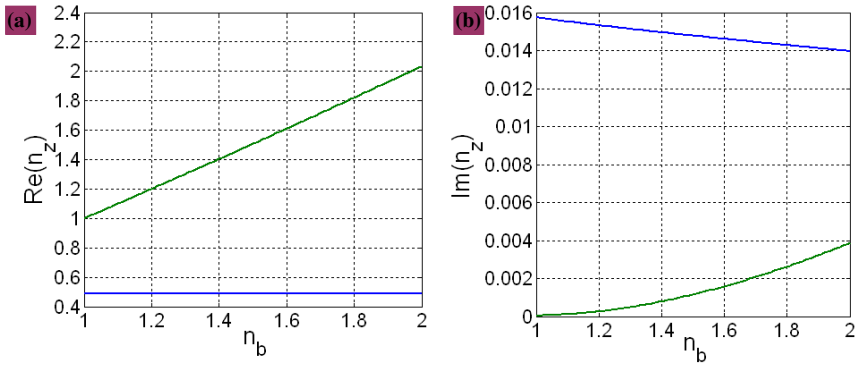

Fig. 11. (a) real and (b) imaginary part of the effective refractive index versus background index. The chosen parameters are: R_c = 0.30 μm, h = 50 nm and λ = 1.55 μm. The green and blue lines are associated to external SPP and core-like mode, respectively.

On the other hand, the Re(n_z) for the core-like mode (blue line) shows very little dependence of the background refractive index. It looks like the metal layer is shielding the core from external effects. However the Im(n_z) shows a slight decrease by increasing n_b.

#152808 - $15.00 USD Received 18 Aug 2011; revised 22 Oct 2011; accepted 25 Oct 2011; published 23 Nov 2011

Figure 12 represents the same kind of calculation as Fig. 11 with R_c = 0.50 μm instead of 0.30 μm. We can observe that for low n_b the modes in the two figures have opposite behavior. In Fig. 11 no intersections are found between the external SPP mode (green line) and the core-like mode (blue line). Furthermore, Re(n_z) of the SPP mode is always higher than that of the core-like mode. In Fig. 12 the situation is quite different. In fact, for low n_b, we can observe an higher value of Re(n_z) for the core-like mode with a close-to-crossing point at n_b~1.2. At this value of the refractive index the two modes exchange their own nature. The core-like one takes a SPP form and the SPP mode turns in core-like mode. The meaning associated to the lines is then opposite on the right and left side of the crossing point n_b~1.2. Hence, the blue line is core-like mode on the left side and SPP on the right side (similarly the green line). What happens at the crossing point is a conversion of the two modes. This is possible because at such a value of n_b the two modes show the same value both for Re(n_z) and Im(n_z). This phenomenon was already observed in Figs. 3 and 6. This shows that n_b has a similar effect as λ, h or R_c: in fact, by changing either these parameters we can have a SPP-to-core mode conversion.

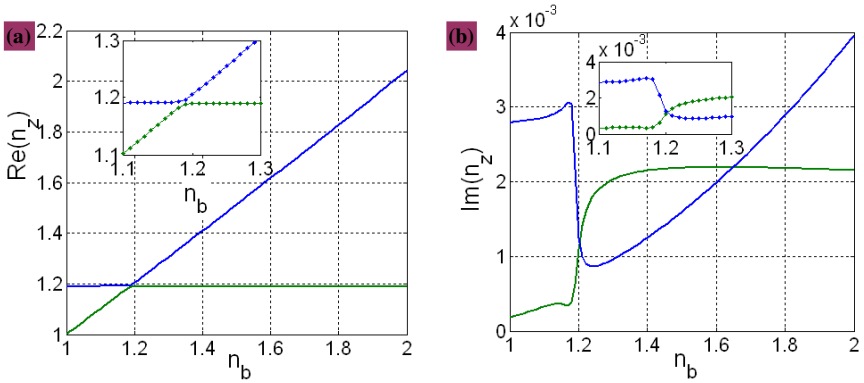

Fig. 12. (a) real and (b) imaginary part of the effective refractive index versus background index. The chosen parameters are: R_c = 0.50 μm, h = 50 nm and λ = 1.55 μm. The insets are the close up view of the crossing points. The dots on the lines represent the calculated points.

4. Super-long SPP modes and gap-mode region

In the previous analysis we have noticed that in some cases the imaginary part of the effective refractive $n_{m,z}$ was very close to zero, such as edge of gap-mode in Figs. 6(d) and 7(b). This means a very long propagation length, namely a loss-free fiber. To explain the origin of this gap we have to recall section 2.1, where we mentioned that in the background (last layer N) the quantity Im($n_{m,t}^{(N)}$) must be always positive in order to have a decaying wave when increasing the radial coordinate $\bar{\rho}$. From Eq. (3) we can get the relation (16), and considering the Im($n_{m,t}^{(N)}$)>0, it can be shown that Re($n_{m,t}^{(N)}$)<0:

$$\begin{cases} \mathrm{Re}^2\left(n_{m,t}^{(N)}\right) - Im^2\left(n_{m,t}^{(N)}\right) = \varepsilon^{(N)}\mu^{(N)} - \mathrm{Re}^2\left(n_{m,z}\right) + Im^2\left(n_{m,z}\right) \\ \mathrm{Re}\left(n_{m,t}^{(N)}\right) Im\left(n_{m,t}^{(N)}\right) = -\mathrm{Re}\left(n_{m,z}\right) Im\left(n_{m,z}\right) \end{cases} \tag{16}$$

In the last external layer of the structure (background) the solution, this is proportional to the Hankel function of the first kind, namely,

$$H_m^{(1)}\left(\bar{\rho}\, n_{m,t}^{(N)}\right) \propto \left[\bar{\rho}\left|n_{m,t}^{(N)}\right|\right]^{-1/2} \exp\left(-i\bar{\rho}\left|\mathrm{Re}\left(n_{m,t}^{(N)}\right)\right|\right) \exp\left(-\bar{\rho}\,\mathrm{Im}\left(n_{m,t}^{(N)}\right)\right) \tag{17}$$

Physically speaking this means a growing wave converge into center of the structure. Square integrate Eq. (17) in external layer, we get

#152808 - $15.00 USD Received 18 Aug 2011; revised 22 Oct 2011; accepted 25 Oct 2011; published 23 Nov 2011

$$\int_N \left| H_m^{(1)}\left(\bar{\rho}\, n_{m,t}^{(N)}\right)\right|^2 \rho d\rho d\varphi \propto \frac{1}{k_0 \,\mathrm{Im}\left(n_{m,t}^{(N)}\right)} \tag{18}$$

From Eq. (16), if Im($n_{m,z}$)→0, then Im($n_{m,t}^{(N)}$)→0, also. This means that most of power distribute in outside. Although the case of Im($n_{m,z}$) = 0 is un-physical, but at least it can be

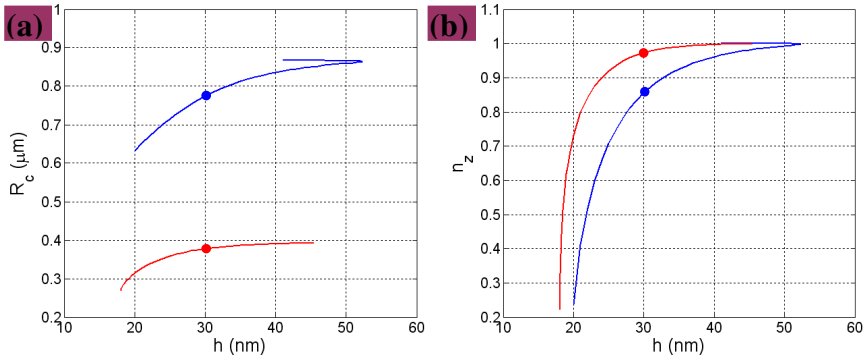

Fig. 13. (a) Relation between SiO_2 core radius and thickness of the silver ring; (b) real part of n_z vs. thickness of the silver ring. The core radius is Rc = 0.3 μm. Both the graphs show only no-loss modes. The wavelength λ = 1.55 μm. The dots represent the calculated modes as in Figs. 14 and 15.

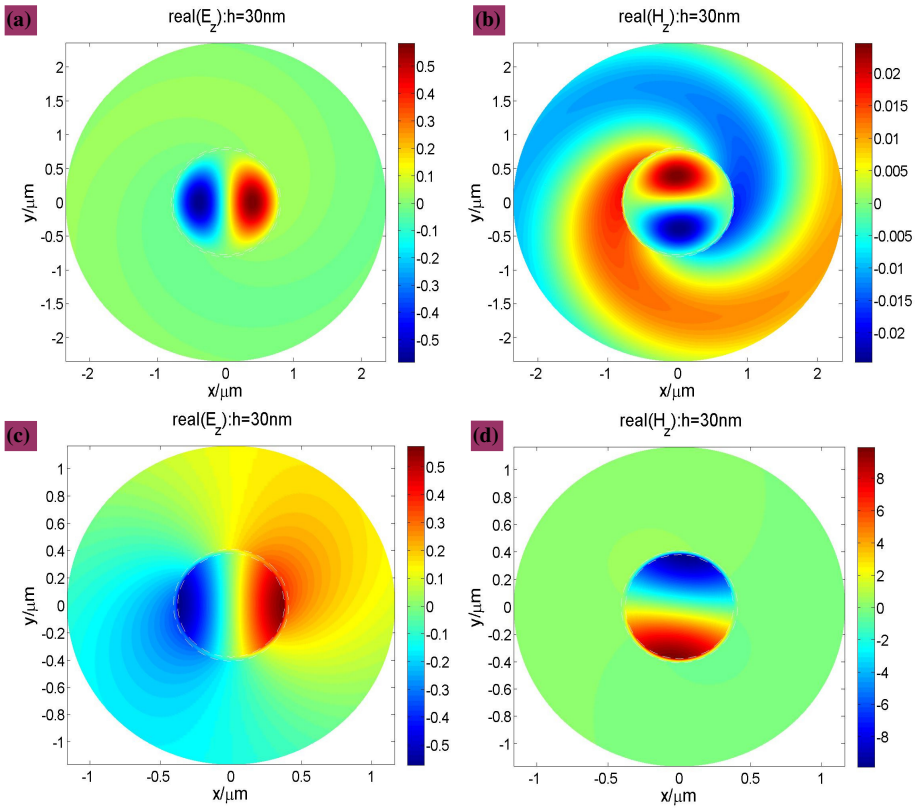

Fig. 14. z component of the electric- and magnetic- field distributions. (a) and (b) are associated to the blue circle of Figs. 13(c) and (d) correspond to the red circle of the same figure. The azimuthal number m = 1.

#152808 - $15.00 USD Received 18 Aug 2011; revised 22 Oct 2011; accepted 25 Oct 2011; published 23 Nov 2011

approached. And it may offer a method for achieve lower loss SPP waveguide. From Fig. 6(d) and Fig. 7(b) we see that the gap regions are dependent on both the radius of core and the thickness of the silver cladding layer. Figure 13(a) summarizes this relation, and Fig. 13(b) shows $n_{m,z}$ (m = 1) versus thickness of the silver ring h (similarly to Fig. 7). The wavelength is taken equal to 1.55 μm.

The z component distributions of the electric- and magnetic- fields are shown in Figs. 14 and 15. The former is associated to the azimuthal number m = 1, the latter to m = −1 (as clearly seen by comparing Figs. 14(b) and 15(b)). In both graphs (a) and (b) correspond to the blue circle of Fig. 13 (similarly, (c) and (d) correspond to the red circle). The silver thickness is fixed at h = 0.30 μm. Even though no SPP modes are observed in Fig. 13, which induces the definition of core-like modes for the Fig. 13, we can see from Figs. 14 and 15 that some of the modes tend to extend far away from the core (see Fig. 14(b) or Fig. 15(b)). This behavior could result useful when light wave transmission is an issue, keeping however in mind that a very strong and sensitive dependence on h and R_c is inherent to these modes.

Finally, we point out one of interesting phenomena, even though we proved above that, the energy almost distribute in external metal layer, however, we can see from Figs. 14 and 15, the field still with strong distribution in inner of core.

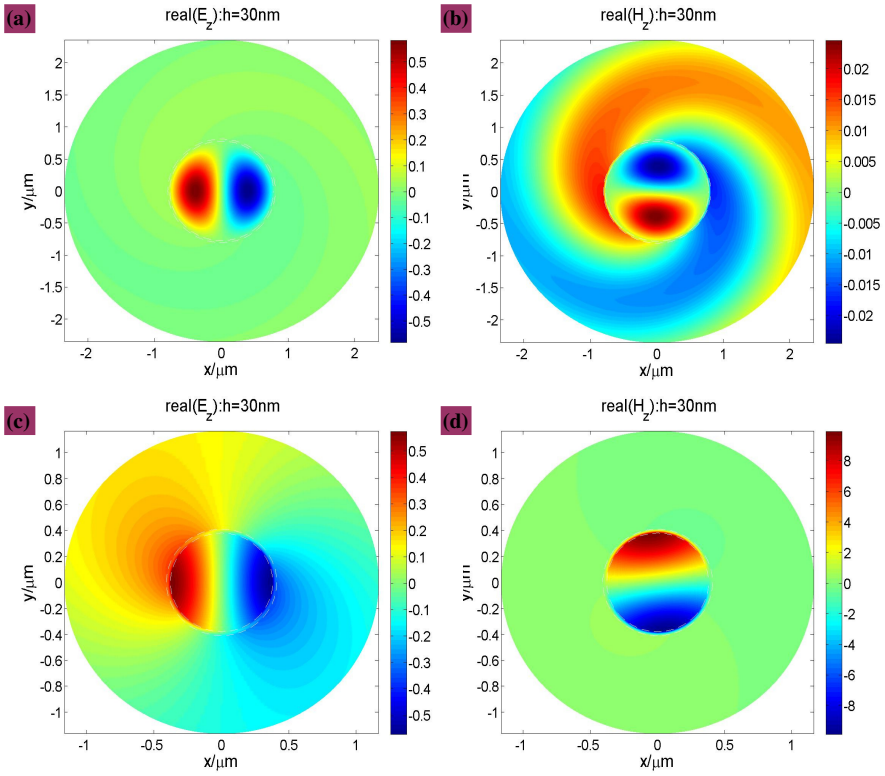

Fig. 15. z component of the electric- and magnetic- field distributions. (a) and (b) are associated to the blue circle of Figs. 13. (c) and (d) correspond to the red circle of the same figure. The azimuthal number m = −1.

5. Subluminal and superluminal light speed

In the dispersion relation of Fig. 3C, the real part of the effective refractive index is strongly dependent on the wavelength, especially at modes coupling region and for values of the effective refractive index close to zero. It offers a momentum for control the light speed. We

#152808 - $15.00 USD Received 18 Aug 2011; revised 22 Oct 2011; accepted 25 Oct 2011; published 23 Nov 2011

can relate it to the *group* refractive index by considering the dispersion of phase refractive index:

$$n_g = n_p\left(1-\frac{\lambda}{n_p}\frac{\partial n_p}{\partial \lambda}\right) \tag{19}$$

Where n_p is phase refractive index and equal to Re(n_z). mode has different group velocity, thus it will induce the mode dispersion. Three kinds of dispersion relations in Fig. 3C are discussed. In Fig. 16 the graphs (a), (b) and (c) correspond to the blue, green and red line in Fig. 3C, respectively. In Fig. 16(a) the maximum value for the group index n_g is close to 18 namely subluminal light speed. This value is found at λ~2.6 μm, which is associated to the flattening of the effective refractive index in the region Re(n_z) close to 0. Moving up in wavelength we observe a decrease of n_g to values below 1, and the opposite situation to the previous case occur, that is superluminal light speed. At λ~1.93 μm we observe a Fano-like shape, as shown in the inset of Fig. 16(a). This describes the external-SPP mode coupling with internal core-like mode.

Figure 16(b) shows the situation for the second dispersion line. The group refractive index amplitude variation is not as strong as Fig. 16(a). The maximum n_g is found at the transition point between core-like and SPP mode. Consistently with Fig. 16(a), in the crossing point of SPP and core-like mode, the n_g shows a ripple.

Finally, Fig. 16(c) describes the two transitions core-SPP and SPP-core for the third dispersion relation curve. Group refractive index n_g can achieve as big as 20. At the coupling region, no strong Fano-like peaks are found, but instead by two of steps. They are at λ~0.65 μm and λ~0.93 μm.

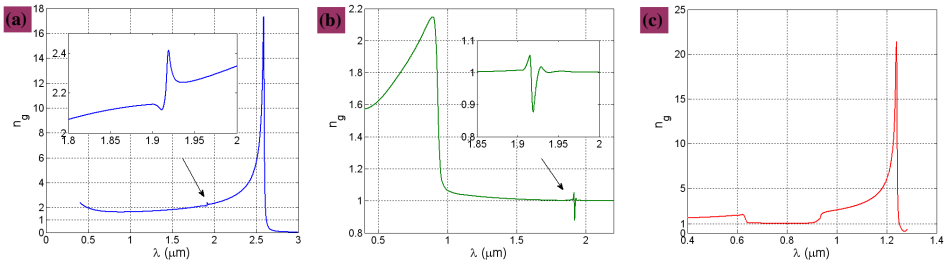

Fig. 16. Group refractive index vs. wavelength. (a), (b) and (c) are associated to the blue, green and red lines in Fig. 3(C), respectively.

6. Conclusion

We have investigated the evolution of the eigenmodes for three kinds of infinitely long cylindrical structures, realized by a combination of metallic and dielectric layers. We have analyzed the modes observing their axial effective complex refractive index. The swinging between core-like and SPP modes has been observed and its strong dependence on optical and geometrical parameters such as λ, h, R_c or n_b has been demonstrated. We displayed the modes evolutions. Furthermore, we have reported on the existence of modes gap. These gaps have shown strong dependence on some geometrical parameters such as R_c and h. Their edges are characterized by showing extremely low loss which, according to the mode kind (core-like or SPP) originates *no-loss* or *super-long* surface plasmon polaritons. Finally, by investigating the wavelength dependence of the group velocity, both superluminal and subluminal regions were identified.

Acknowledgments

This work was supported by the program for New Century Excellent Talents at University of China (NCETU) and by SERC/ASTAR/Singapore.

#152808 - $15.00 USD Received 18 Aug 2011; revised 22 Oct 2011; accepted 25 Oct 2011; published 23 Nov 2011